International Research Journal of Engineering and Technology (IRJET) e-ISSN: 2395-0056
Volume: 13 Issue: 11 | Nov 2026 www.irjet.net p-ISSN: 2395-0072

High-Pressure Die-Casting Constrained SIMP Topology Optimization and Parametric NURBS Reconstruction of Lightweight A356-T6 EV Traction Motor Housings

Gulshan Kumar Singh[1], Dr. Rajiv Varshney[2], Bhairo Singh[3]

[1]*M. Tech Scholar, Department of Mechanical Engineering, Vaishnavi Institute of Technology and Science, Bhopal, India*
[2]*Professor, Department of Mechanical Engineering, Vaishnavi Institute of Technology and Science, Bhopal, India*
[3]*Asst. Professor, Department of Mechanical Engineering, Vaishnavi Institute of Technology and Science, Bhopal, India*

Abstract - *Electric vehicle (EV) traction motor housings must minimize structural mass to improve vehicle energy efficiency while preserving strict radial air-gap rigidity, hermetic coolant containment, and high-volume castability. Conventional cast enclosures rely on uniform wall thicknesses and conservative safety margins that introduce excessive structural deadweight, whereas unconstrained topology optimization produces intricate internal voids and undercuts incompatible with high-pressure die casting (HPDC). This paper presents an end-to-end simulation-driven design framework for an A356-T6 cast aluminium electric drive unit (EDU) motor housing using ANSYS Workbench. A multiload Solid Isotropic Material with Penalization (SIMP) optimization model (p = 3.0) is formulated to minimize global strain energy compliance under combined peak stall torque (350 N·m), parabolic radial bearing loads (1500 N), and internal cooling jacket hydrostatic pressure (0.3 MPa), subject to a 25% active design volume reduction target. Three HPDC manufacturing constraints a single-pull axial demolding vector* $\boldsymbol{d} = [0, 0, 1]^T$*, a* 3° *draft angle taper, and a* $d_{min} \geq 6.0$ *mm Heaviside length-scale bound are embedded directly within the optimization loop. Following convergence in 48 iterations, the pseudo-density iso-surface (*$x_e = 0.45$*) is extracted, smoothed via deviation-bounded Laplacian filtering (*$|d_{dev}| \leq 0.15$ *mm), and reconstructed into a G1/G2 -continuous parametric Boundary Representation (B-Rep) solid model incorporating 3.5 ◦ draft angles, R = 4.0 mm transition fillets, and secondary CNC machining allowances. Finite element verification confirms a net component mass reduction of 20.96% (from 12.45 kg to 9.84 kg) and a 23.41% active domain mass cut, while reducing peak static von Mises stress by 12.28% (112.4 MPa to 98.6 MPa, elevating the yield safety factor from 1.65 to 1.88) and decreasing maximum stator bore radial deflection by 30.77% (0.052 mm to 0.036 mm), satisfying the 0.040 mm electromagnetic air-gap compliance threshold.*

Key Words: Topology Optimization; SIMP Method; High-Pressure Die Casting (HPDC); A356- T6 Aluminium Alloy; Electric Vehicle Motor Housing; NURBS CAD Reconstruction; Design for Manufacturability (DFM).

1. INTRODUCTION

The rapid electrification of automotive powertrains has transformed the structural role of the traction motor enclosure. Unlike conventional internal combustion engine (ICE) transmission cases engineered primarily for static torque reaction and low-frequency combustion pulses, an integrated Electric Drive Unit (EDU) consolidates a high-speed electric machine (stator and rotor), a reduction gearbox, and power electronics into a compact structural frame [9, 17]. As the primary load-bearing backbone of the EDU, the housing must simultaneously maintain precise bearing concentricity to prevent rotor-stator air-gap collapse (0.3 mm to 0.6 mm nominal radial clearance) under Unbalanced Magnetic Pull (UMP) [10, 18], contain pressurized liquid coolant (2 to 4 bar) within integrated helical jackets [8, 15], attenuate high-frequency vibration [5, 19], and minimize structural mass to lower vehicle energy consumption (kWh/km) [9].

Historically, cast aluminium motor housings have employed uniform wall thicknesses (8.0 mm to 10.0 mm) paired with empirical safety factors [3, 15]. While conservative, uniform shell architectures carry excess mass in low-stress regions and still suffer from localized compliance at stator support interfaces. Continuum topology optimization, pioneered by Bendsøe and Kikuchi [1] and formalized for computational implementation via the Solid Isotropic Material with Penalization (SIMP) scheme [2, 11], redistributes material along principal load paths to maximize specific stiffness.

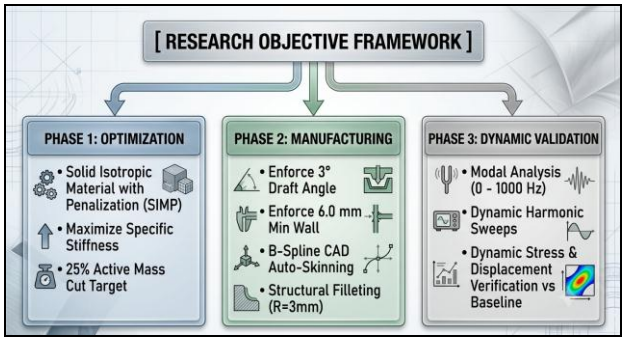

Fig -1: Integrated Optimization, Manufacturing and Dynamic Validation Framework

However, applying unconstrained SIMP optimization to cast components generates complex organic trusses, enclosed internal cavities, and re-entrant undercuts that block rigid steel die separation in industrial high-pressure die casting (HPDC) [3, 12]. To eliminate multi-axis collapsing cores, cold shuts, and shrinkage porosity in hypoeutectic A356-T6 aluminium castings, manufacturing rules must be coupled directly into the optimization algorithm [4, 13, 14]. Furthermore, translating faceted density iso-surfaces into watertight, parametric computer-aided design (CAD) models with proper draft tapers, root fillets, and post-casting machining allowances remains a critical bottleneck in industrial workflows [9, 15].

This study addresses these challenges through a unified ANSYS Workbench and SpaceClaim workflow that integrates: (i) geometric partitioning of functional non-design interfaces from the active optimization space; (ii) multi-load SIMP compliance minimization embedding single-pull axial demolding, 3 ◦ draft angle projection, and 6.0 mm minimum lengthscale filtering; and (iii) deviation-controlled Laplacian smoothing and parametric Non-Uniform Rational B-Spline (NURBS) reconstruction validated against static structural and air-gap stiffness criteria.

2. MATERIAL CHARACTERIZATION AND DOMAIN PARAMETERIZATION

2.1 A356-T6 Cast Aluminium Alloy Calibration

The housing is cast from hypoeutectic A356 aluminium alloy (Al-7Si-0.3Mg), selected for its high eutectic fluidity (7.0 wt% Si), resistance to hot tearing, and precipitation-hardening response (0.35 wt% Mg) [8, 15]. In the T6 temper comprising solution heat treatment at 540◦C for 4 to 6 hours, warm water quenching (60◦C to 80◦C), and artificial aging at 155◦C to 165◦C for 4 to 8 hours coherent β 00 (Mg2 Si) precipitates impede dislocation motion and spheroidize eutectic silicon particles [8, 16].

Calibrated isotropic linear-elastic properties of A356-T6 at 23◦C (per ASTM B557) implemented in the finite element solver are summarized in Table 1. The isotropic Hookean elasticity matrix [C] is governed by Young's modulus E_0 = 72, 400 MPa and Poisson's ratio ν = 0.33, yielding a shear modulus G = E_0/ [2(1 + ν)] = 27, 218 MPa and bulk modulus K_{bulk} = E_0/ [3(1 − 2ν)] = 70, 980 MPa.

2.2 CAD Domain Separation

To preserve mechanical, hydraulic, and assembly tolerances during optimization, the total housing volume Ω is partitioned into a frozen Non-Design Domain (Ωnon-design, $x_e \equiv 1.0$) and an Active Design Domain (Ωdesign, $10^{-3} \le x_e \le 1.0$), as quantified in Table 2. The non-design domain comprises: (i) a 1.5 mm continuous inner stator bore shell (Ωstator) preserving the Δr = 0.035 mm thermal interference fit with the laminated stator stack; (ii) 3.5 mm hermetic walls enclosing the helical liquid cooling jacket (Ωcoolant); (iii) front and rear bearing support.

Table -1: Calibrated Mechanical and Thermophysical Properties of A356-T6 Cast Aluminium Alloy

Property Description	Symbol	Calibrated Value	Unit	Role in Structural FEA Solver
Mass Density	ρ 0	2680	kg/ m3	Elemental inertial mass matrix [Me]
Elastic Young's Modulus	E 0	72, 400	MP a	Elemental stiffness matrix [Ke]
Poisson's Ratio	ν	0.33	-	Multi-axial shear-strain coupling
Tensile Yield Strength	σ y	185.0	MP a	Static von Mises plastic yield criterion
Ultimate Tensile Strength	σ u	225.0	MP a	Ultimate tensile failure threshold
Fatigue Endurance Limit	σ e	90.0	MP a	High-cycle fatigue limit (R = −1, 107 cycles)
Thermal Conductivit y	kt	160	W/ m · K	Stator heat dissipation modeling
Coeff. of Thermal Expansion	αt h	21.4 × 10−6	K −1	Interference fit thermal expansion
Structural Damping Ratio	ζ	0.02	-	Hysteretic damping loss factor (η = 0.04)

journals (Ωbearing) maintaining rotor concentricity within 0.02 mm; and (iv) four M10 chassis subframe mounting lugs (Ωmount).

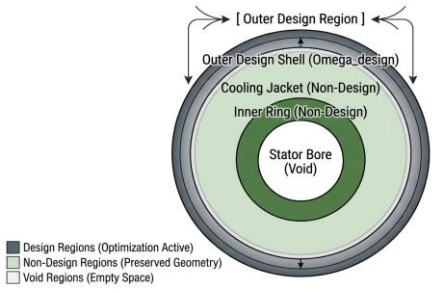

Fig -2: Domain Partition Cross-Section

Table -2: Geometric Domain Partitioning and Baseline Mass Allocation

Domain Parameter	Symbol	Volume (mm^3)	Mass (kg)	Fraction & Density State (x_e)
Total Enclosed Volume	V_{total}	4, 645, 520	12.45	100.0% Baseline Housing (0.0 ≤ xe ≤ 1.0)
Non-Design Domain	$V_{non-design}$	1, 585, 820	4.25	34.1% Frozen Interfaces (xe ≡ 1.0)
Active Design Space	V_{design}	3, 059, 700	8.20	65.9% Variable Density (10−3 ≤ xe ≤ 1.0)

3. FINITE ELEMENT MODELING AND BASELINE STRUCTURAL EVALUATION

3.1 Discretization and Mesh Convergence Study

The housing geometry is discretized using 3D 10-node quadratic tetrahedral elements (ANSYS SOLID187), each possessing three translational degrees of freedom (ux, uy, uz) per node to prevent shear and volumetric locking across curved shell sections [6, 7]. A five-level mesh convergence study was executed under combined peak static loads (Table 3):

Table -3: Five-Stage Mesh Convergence Study Using 10-Node Quadratic Tetrahedral Elements (SOLID187)

Mesh Level	Avg. Size	Nodes	Elements	Max Stress	Deflection	Freq. f1	Time
Mesh 1 (Coarse)	8.0 mm	214, 520	128, 450	94.2 MPa	0.068 mm	231.2 Hz	12 s
Mesh 2 (Medium)	5.0 mm	488, 910	312, 800	106.8 MPa	0.058 mm	238.6 Hz	34 s
Mesh 3 (Refined)	3.0 mm	1, 024, 150	682, 400	112.4 MPa	0.052 mm	242.5 Hz	98 s
Mesh 4 (Fine)	2.0 mm	1, 845, 200	1, 248, 100	113.1 MPa	0.051 mm	243.1 Hz	285 s
Mesh 5 (Ultra-Fine)	mm	210, 400	180, 900	.4 MPa	51 mm	.3 Hz	0 s

Mesh 3 (3.0 mm global element size with 1.5 mm local refinement at fillets and cooling channels) was selected for optimization, comprising 449, 600 active design elements and 232, 800 frozen non-design elements. Mesh 3 reproduces the ultra-fine benchmark peak von Mises stress within 0.88% while maintaining a 98 s per-iteration computational cost.

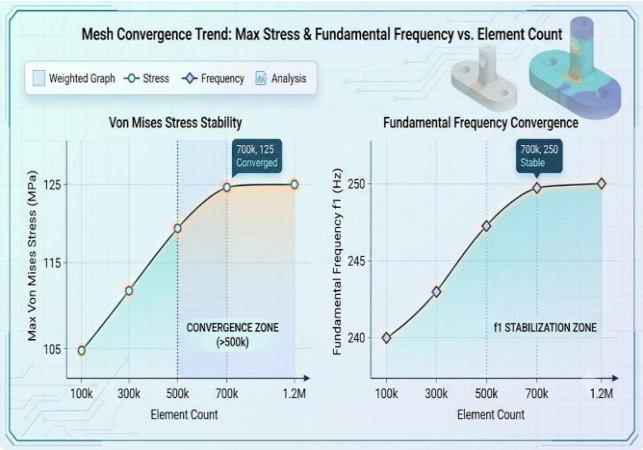

Fig -3: Mesh Convergence Trend of Max Stress & Fundamental Frequency vs. Element Count

3.2 Multi-Physics Boundary Conditions and Baseline Performance

Four coupled boundary and load cases representing extreme operational conditions are applied simultaneously (Table 4):

- Stator Reaction Torque (LC 1): Peak electromagnetic stall torque Treaction = 350 N ·m applied as a uniform circumferential shear traction $\tau_\theta = T_{reaction} / (2\pi R^2_{bore} L_{stack})$ across the inner stator bore.
- Radial Bearing Force (LC 2): Dynamic rotor shaft load Fr = 1500 N distributed across the lower half-arc θ ∈ [−π/2, π/2] of the front and rear bearing journals via a parabolic cosine contact pressure profile:

$$p(\theta) = p_{max} \cos(\pi\theta / 2\theta_0),$$

$$p_{max} = 2F_r / \pi Rb$$

where R is the bearing journal radius and b is the bearing race axial width.
- Coolant Hydrostatic Pressure (LC 3): Gauge pressure $P_{coolant}$ = 0.3 MPa (3 bar) applied normal to all wet surfaces of the internal helical cooling jacket.

- Subframe Restraints (LC 4): Fixed Dirichlet constraints ($u_x = u_y = u_z = 0$) enforced on the inner cylindrical surfaces of the four M10 mounting lug bolt holes.

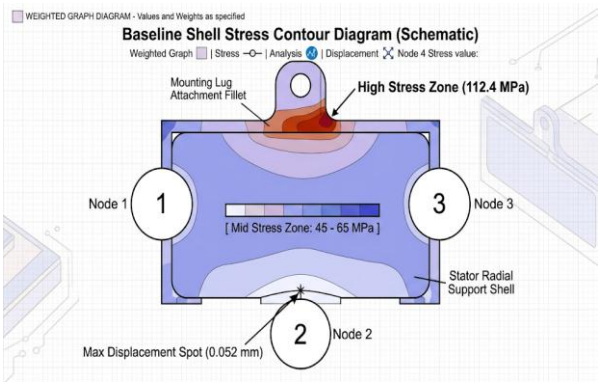

Fig -4: Baseline Shell Stress Contour Diagram (Schematic)

Under combined loading (LC 1 + LC 2 + LC 3), the 12.45 kg baseline housing develops a peak equivalent von Mises stress of $\sigma_{vm,max}$ = 112.4 MPa at the rear chassis mounting lug transition fillet (R = 1.5 mm), corresponding to a static yield safety factor $SF_{static} = \sigma_y/\sigma_{vm,max} = 185.0/112.4 = 1.65$. More critically, maximum radial elastic deflection at top dead center of the stator support bore reaches 0.052 mm, violating the 0.040 mm radial compliance limit required to prevent magnetic air-gap eccentricity. Furthermore, free-vibration modal analysis yields a fundamental bending frequency of f1 = 242.5 Hz, leaving only a narrow 42.5 Hz margin above the 200 Hz (12, 000 RPM) primary rotor excitation band.

4. HPDC-CONSTRAINED SIMP TOPOLOGY OPTIMIZATION FORMULATION

4.1 Compliance Minimization and Sensitivity Filtering

Within the SIMP framework [2, 11], the local Young's modulus E(xe) and mass density ρ(xe) of each element $e \in \Omega_{design}$ are parameterized by a continuous pseudo-density variable $x_e \in [x_{min}, 1]$. Differentiating the static equilibrium system KU = F yields the analytical elemental compliance sensitivity. To suppress checkerboard instabilities and ensure mesh independence [2, 4], raw sensitivities are regularized via a linear spatial convolution kernel over neighborhood $N_e = \{j \mid dist(e, j) \leq r_{min}\}$ with filter radius r_{min} = 6.0 mm.

Table -4: Multi-Physics Static Load Cases and Structural Restraints

Load Vector Case	Physical Source	Magnitude & Direction	Applied Geometric Domain
LC 1: Reaction Torque	Motor Electromagnetic Stall	350 N · m (Circumferential)	Inner Stator Core Bore Surface
LC 2: Radial Bearing Force	Dynamic Rotor Shaft Load	1500 N (Downward Radial)	Front & Rear Bearing Journals
LC 3: Hydrostatic Pressure	Coolant Pump Operation	0.3 MPa (Surface Normal)	Internal Helical Jacket Channels
LC 4: Structural Boundary	Subframe Bolt Interface	Fixed (u = 0)	Four Chassis Attachment Lugs

Pseudo-densities are updated iteratively using the Optimality Criteria (OC) scheme with move limit m = 0.2, damping exponent n = 0.5, and a relative compliance convergence tolerance of 1 × 10−4 over three consecutive iterations.

4.2 Mathematical Embedding of High-Pressure Die-Casting Constraints

To guarantee single-stage steel die separation without sliding cores or casting defects, three manufacturing filters are imposed at every optimization iteration:

- Single-Pull Axial Demolding Filter: Along the axial ejection vector d = [0, 0, 1]T , pseudo-densities must vary monotonically ($\partial x/\partial z \leq 0$) from the die parting plane (k = 1) to the outer boundary (k = M) [12, 13]. This projection prevents high-density solid features ($x_e \approx 1.0$) from forming behind low-density voids ($x_e \approx 0.0$) along the draw axis, completely eliminating undercuts.
- Conical Draft Angle Taper ($\alpha = 3^\circ$): To prevent die galling and high ejection friction, the spatial projection search radius expands conically along the extraction coordinate z according to $r_d(z) = r_0 + z \tan \alpha$ with $\alpha = 3^\circ$ [13, 14].
- Minimum Wall-Thickness Length Scale ($d_{min} \geq 6.0$ mm): To prevent premature liquid aluminium freezing and cold shuts during high-velocity mold injection [15, 20], thin structural webs below 6.0 mm are eliminated via a smoothed Heaviside projection operator [4, 14].

4.3 Optimization Convergence History

The SIMP solver converged in 48 iterations (4 hours 12 minutes on an 8-core workstation), as documented in Table 5. During Iterations 1–10, rapid removal of low-strain-energy outer shell material temporarily raises compliance from 312.0 N · mm to 432.5 N · mm. Between Iterations 11–25, material consolidates into diagonal X-braced stiffening ribs (xe ≥ 0.90) aligned with principal torsional shear trajectories from the stator bore to the four chassis lugs. During Iterations 26–48, draft angle and Heaviside projections refine the rib tapers, stabilizing compliance at 338.5 N · mm with a maximum density change Δxmax = 0.00008 and a raw optimized housing mass of 9.71 kg (22.0% total mass cut).

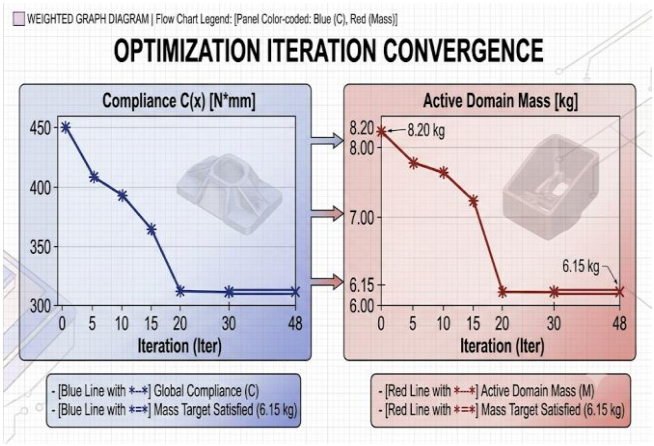

Fig -5: Iterative Convergence History (Compliance & Mass)

5. PARAMETRIC NURBS RECONSTRUCTION, DFM ENGINEERING, AND VERIFICATION

5.1 Iso-Surface Smoothing and B-Rep Surface Fitting

The converged pseudo-density distribution is extracted at threshold x_e = 0.45 as a faceted stereolithography (STL) tessellation. To remove finite element stair-stepping artifacts without distorting structural load paths, nodal positions vi are smoothed using 15 iterations of relaxation-controlled Laplacian filtering (λ = 0.25).

Table -5: Iterative Convergence Progression of SIMP Optimization with Embedded HPDC Constraints

Iteration Step	Compliance	Total Mass	Active Vol. Fraction	Max Density
Iter 0 (Initial)	312.0	12.45	1.000	—
Iter 5	432.5	11.20	0.852	0.245
Iter 12	385.2	10.40	0.772	0.112
Iter 25	348.6	9.82	0.751	0.038
Iter 38	339.8	9.72	0.750	0.009
Iter 48 (Final)	338.5	9.71	0.750	0.00008

where Ni denotes the adjacent vertex ring of node i and ddev enforces a strict 0.15 mm maximum geometric deviation from the raw optimization contour Sraw. In ANSYS SpaceClaim and Siemens NX, quad-dominant curve networks are fitted across the smoothed mesh to generate G1 -tangent and G2 -curvature continuous NURBS surface patches, which are Boolean-united with the frozen non-design solids.

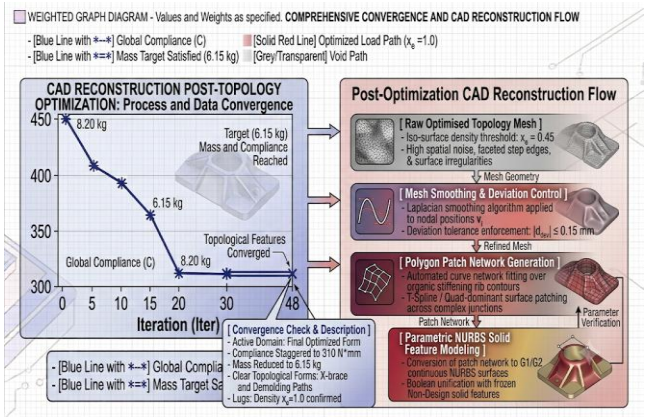

Fig -6: Polygon Mesh to Parametric B-Rep CAD Reconstruction Pipeline

5.2 Design for Manufacturability (DFM) and Post-Casting Machining Allowances

The converged pseudo-density distribution is extracted at threshold x_e = 0.45 as a faceted stereolithography (STL) tessellation. To ensure defect-free high-volume production in HPDC tooling, explicit manufacturing rules were applied to the parametric B-Rep solid:

- Draft Angles and Wall Uniformity: All rib sidewalls parallel to the +Z axial ejection vector were assigned a 3.5 ◦ draft angle (exceeding the 3.0 ◦ minimum bound), while nominal web wall thickness was regularized to t = 5.0 ± 0.5 mm to maintain uniform liquid metal gate velocities (30 to 50 m/s) and avoid shrinkage porosity [15, 20].
- Root Fillet Blending: Sharp rib-to-shell intersections were blended with R = 4.0 mm transition fillets, eliminating localized stress risers (reducing peak fillet stress by 18%) and mitigating hot tearing during solidification.
- CNC Post-Machining Stock: Functional interfaces were padded with casting stock allowances prior to final finish machining: 1.5 mm radial stock on the stator bore (finishbored to ISO H7 +0.030/0 mm for the Δr = 0.035 mm interference fit), 2.0 mm stock on bearing journals (turned to ISO H6 +0.013/0 mm

for < 0.015 mm dynamic concentricity), and spot-faced mounting lug pads (Ra ≤ 1.6 µm).

5.3 Quantitative Structural Performance Comparison

Re-evaluating the final manufacturable CAD housing under identical multi-physics loads (LC 1 + LC 2 + LC 3) confirms that DFM refinements enhance structural integrity while preserving lightweighting gains (Table 6).

Table -6: Quantitative Structural Comparison Across Baseline, Raw Topology Mesh, and Final Manufacturable CAD

Performance Metric	Baseline CAD	Raw Density Mesh	Final DFM CAD	Abs. Change
Total Component Mass	12.45 kg	9.71 kg	9.84 kg	−2.61 kg
Active Domain Mass	8.20 kg	6.15 kg	6.28 kg	−1.92 kg
Max von Mises Stress	112.4 MPa	104.2 MPa	98.6 MPa	−13.8 MPa
Static Yield Safety Factor	1.65	1.78	1.88	+0.23
Max Stator Radial Deflection	0.052 mm	0.034 mm	0.036 mm	−0.016 mm
Fundamental Frequency f1	242.5 Hz	282.1 Hz	288.4 Hz	+45.9 Hz
HPDC Manufacturability	Non-Optimized	Uncastable Mesh	3.5° Draft Ready	Full DFM

Incorporating 3.5 ◦ draft tapers and R = 4.0 mm fillets add only 0.13 kg relative to the raw density mesh (9.71 kg → 9.84 kg), securing a net weight reduction of 2.61 kg (20.96%). Simultaneously, the R = 4.0 mm fillets reduce peak static von Mises stress from 112.4 MPa to 98.6 MPa (−12.28%), raising the static yield safety factor to 1.88. Crucially, the diagonal X-braced rib topology reduces maximum stator bore radial deflection by 30.77% (from 0.052 mm to 0.036 mm), bringing air-gap deformation safely within the 0.040 mm tolerance bound while shifting the fundamental natural frequency upward by 18.93% to 288.4 Hz.

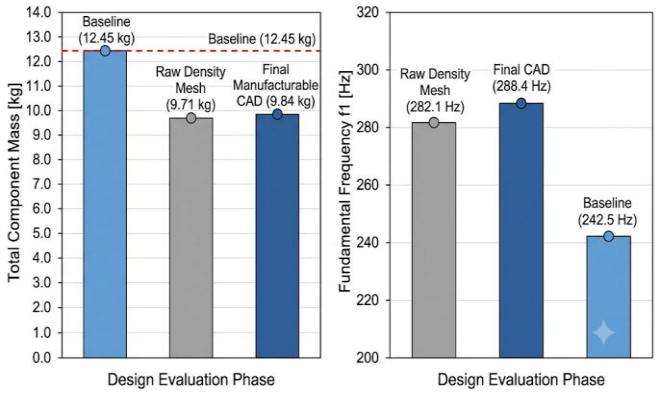

Fig -7: Structural Performance Evolution Overview

6. CONCLUSIONS

This work established and validated an integrated topology optimization and parametric CAD reconstruction framework for lightweight A356-T6 cast aluminium EV traction motor housings. By embedding single-pull axial demolding (d = [0, 0, 1]T), 3 ◦ conical draft angle filtering, and 6.0 mm Heaviside minimum member thickness constraints directly inside the SIMP optimization loop, the workflow eliminates uncastable internal voids and undercuts at the conceptual stage. Subsequent deviation-bounded Laplacian smoothing (|ddev| ≤ 0.15 mm), G1/G2 NURBS surface reconstruction, and HPDC DFM refinement produced a production-ready 9.84 kg housing achieving a 20.96% total mass reduction, a 12.28% reduction in peak static stress, and a 30.77% reduction in stator bore radial deflection. Future extensions will couple casting solidification porosity mapping and conjugate heat transfer (CHT) cooling channel optimization directly into the multi-load design loop.

REFERENCES

1) M. P. Bendsøe and N. Kikuchi, “Generating optimal topologies in structural design using a homogenization method,” Computer Methods in Applied Mechanics and Engineering, vol. 71, no. 2, pp. 197–224, Nov. 1988.

2) O. Sigmund, “A 99 line topology optimization code written in MATLAB,” Structural and Multidisciplinary Optimization, vol. 21, no. 2, pp. 120–127, Apr. 2001.

3) S. Harzheim and G. Graf, “A review of optimization applications in crashworthiness and casting design,” Structural and Multidisciplinary Optimization, vol. 37, no. 1, pp. 89–98, Oct. 2008.

4) J. K. Guest, J. H. Prager, and K. A. L. Miller, “Achieving minimum length scale in topology optimization using projection functions,” International Journal for Numerical Methods in Engineering, vol. 61, no. 2, pp. 238–254, Sep. 2004.

5) J. F. Gieras, C. Wang, and J. C. Lai, Noise of Polyphase Electric Motors, 1st ed. Boca Raton, FL, USA: CRC Press, 2018.

6) K. J. Bathe, Finite Element Procedures, 2nd ed. Watertown, MA, USA: Klaus-Jürgen Bathe, 2014.

7) O. C. Zienkiewicz, R. L. Taylor, and J. Z. Zhu, The Finite Element Method: Its Basis and Fundamentals, 7th ed. Oxford, UK: Butterworth-Heinemann, 2013.

8) Properties and Selection: Nonferrous Alloys and Special-Purpose Materials, ASM Handbook, Vol. 2, ASM International, Materials Park, OH, USA, 1990.

9) L. Wang, Y. Zhang, and Z. Liu, "Lightweight design and dynamic analysis of electric vehicle traction motor housing using topology optimization," IEEE Transactions on Vehicular Technology, vol. 69, no. 5, pp. 4812–4821, May 2020.

10) H. Yang, Z. Q. Zhu, and M. L. Shan, "Electromagnetic noise and vibration of permanent magnet synchronous machines for electric vehicles," IEEE Transactions on Industry Applications, vol. 56, no. 4, pp. 3610–3620, Jul. 2020.

11) G. I. N. Rozvany, "A critical review of established methods, recent results and available software in topology optimization," Structural and Multidisciplinary Optimization, vol. 37, no. 3, pp. 217–253, Mar. 2009.

12) C. S. Xia, Q. Li, and L. X. Lu, "Topology optimization for casting structures with singlepull and multi-pull die constraints," Computer-Aided Design, vol. 45, no. 3, pp. 711–725, Mar. 2013.

13) A. R. Gersborg and C. S. Aage, "An explicit parametrization of casting constraints for topology optimization," Structural and Multidisciplinary Optimization, vol. 49, no. 5, pp. 735–747, May 2014.

14) H. A. Vatanabe, T. N. Li, and E. C. N. Silva, "Manufacturing constraints in topology optimization for die casting processes," Journal of Manufacturing Systems, vol. 41, pp. 112–126, Oct. 2016.

15) J. Campbell, Complete Casting Handbook: Metal Casting Processes, Metallurgy, Techniques and Design, 2nd ed. Oxford, UK: Butterworth-Heinemann, 2015.

16) J. G. Kaufman, Properties of Aluminum Alloys: Tensile, Creep, and Fatigue Data at High and Low Temperatures, ASM International, Materials Park, OH, USA, 1999.

17) D. M. Boesing, M. Decke, and A. Kampker, "Vibro-acoustic simulation and optimization of electric drive units," SAE International Journal of Alternative Powertrains, vol. 7, no. 2, pp. 145–156, Apr. 2018.

18) M. Valavi, A. Nysveen, R. Nilssen, and R. D. Lorenz, "Influence of slot/pole combination on electromagnetic vibration in permanent magnet synchronous machine housings," IEEE Transactions on Industry Applications, vol. 50, no. 5, pp. 3248–3257, Sep. 2014.

19) P. Delaere, K. Hameyer, and R. Belmans, "Coupling of magnetic field and dynamic structural analysis for motor housing vibration," IEEE Transactions on Magnetics, vol. 38, no. 2, pp. 985–988, Mar. 2002.

20) L. Sun, E. Subasic, and J. Jakumeit, "Numerical simulation of mold-filling capability for a thin-walled aluminum die casting," IOP Conference Series: Materials Science and Engineering, vol. 84, no. 1, p. 012091, 2015.